

Differentially rotating magnetised neutron stars: production of toroidal magnetic fields

A.V. Thampan

Inter–University Centre for Astronomy and Astrophysics (IUCAA), Pune 411 007, India e-mail: arun@iucaa.ernet.in

Abstract. We initiate numerical studies of differentially rotating magnetised (proto) neutron stars by studying - through construction from first principles - the coupling between an assumed differential rotation and an impressed magnetic field. For a perfect incompressible, homogeneous, non-dissipative fluid sphere immersed in an ambient plasma, we solve the (coupled) azimuthal components of the Navier-Stokes equation and the Maxwell induction equation. The assumed time-independent poloidal field lines get dragged by the rotating fluid and produce toroidal magnetic fields. Surface magnetic fields take away energy redistributing the angular momentum to produce rigid rotation along poloidal field lines. Due to absence of viscous dissipation, sustained torsional oscillations are set up within the star. However, the perpetual oscillations of neighbouring ‘closed’ field lines get increasingly out of phase with time, leading to structure build up as in Liu & Shapiro (2004) implying the importance of taking into account diffusion (Spruit 1999) for realistic modeling.

Key words. gravitational waves – MHD – stars:neutron – stars:rotation – stars: magnetic fields

1. Introduction

Absence of short period ($\lesssim 1$ ms) newborn radio pulsars (see e.g. Bhattacharya & Van den Heuvel 1991) is a long standing conundrum of pulsar physics. Mechanisms for spinning down the protoneutron star – the object left behind immediately (3–4 s) after a supernova explosion or a binary neutron star merger event – over dynamical timescales, therefore, assume significance in modeling these objects. The proposed mechanisms of spin-down are through the emission of gravitational waves (e.g. Lindblom, Owen & Morsink 1998), or through magnetic braking or viscous damping (Heger et al 2003). Other processes that rely on instabilities (e.g. Andersson 2003; Spruit & Phinney 1998) for spinning down the star have also received attention. An important ingredient in all these mechanisms is the differential rotation of the object. Differential rotation is expected to be strong in the first few seconds after the supernova collapse (Akiyama et al. 2003) – this can be the case even following a neutron star–neutron star binary merger (Zwergner & Muller 1997; Rampp, Muller & Ruffert 1998), although such a binary merger results in a black-hole formation, following a short lived “hypermassive” neutron star stage (e.g. Shibata & Uryu 2000, Rasio & Shapiro 1999). Amongst the above mechanisms, the spin down of neutron stars through gravitational wave emission as a consequence of r-mode oscillations have aroused particular interest in recent years (Lindblom, Owen & Morsink 1998). Particularly, there have been suggestions that neutron stars with superfluid cores and/or solid crusts could be sources for gravitational waves, spinning down young neutron stars to the observed pulsar periods (Andersson & Kokkotas 2001). The interest in r-mode instability is due to the possibility of the frequency and amplitude of the gravitational waves being in the observable range of upcoming and operational gravitational wave detectors like LIGO, VIRGO, TAMA, GEO (Heger et al 1998). However, r-modes can suffer suppression or damping in the presence of hyperon bulk viscosity (Jones 2001; there nonetheless exist “windows of opportunity” – Andersson & Kokkotas 2001) or magnetic fields (Rezzolla, Lamb & Shapiro 2000; Rezzolla et al 2001a,b), in addition, it was recently shown (Arras et al. 2003) that the saturation energies of r-modes are extremely small to account for the spin-down to periods of the order of 10–100 ms. The damping timescales of differential rotation, varies from 10^{-3} s for r-modes, to 10^3 s for Alfvén effects or 10^9 s for molecular viscosity. Thus, it is of pertinence for pulsar physics, as well as gravitational wave physics, to establish which of the above effects dominate and at what timescales they take effect.

Although a magnetic field of 10^{13} G is expected by flux conservation of the magnetic field of the progenitor star, the exact evolution to a cold rigidly rotating object with a predominantly dipole magnetic field of the above magnitude is still a controversial issue (e.g. Chanmugam, Rajasekhar & Young 1995 and references therein). The issue is complicated due to observations (for at least one pulsar) of higher multipole components (Gil & Mitra 2001). The subsequent evolution of the magnetic field of the radio pulsar (Srinivasan et al 1990, Ruderman, M. 1991 a,b,c, Blandford, Applegate & Hernquist, L. 1983, Sang & Chanmugam 1987, Geppert & Urpin 1994, Urpin & Geppert 1995,1996, Konar & Bhattacharya 1997, Konar & Bhattacharya 1999, Mitra, Konar & Bhattacharya 1999, see Bhattacharya 2002 for a recent review), thus, crucially depends on the magnetic field (and the rotation rate) that the pulsar possesses as soon as it is ‘switched on’ (Vivekanand & Narayan 1981). These effects acquire additional significance when gravitational effects are taken into account (Rezzolla, Ahmedov & Miller 2001; Zanotti & Rezzolla 2002).

A possible mechanism to slow down the pulsar is through the production of interior toroidal magnetic field components (from poloidal components through differential rotation) and back reaction of this on the rotational flow. Moffatt (1978) discussed the distortion of an initially uniform magnetic field by differential rotation and showed that a net toroidal magnetic field flux over the entire space covering the interior of the star to infinity, can develop only as a result of diffusion and only if the term $\rho(\mathbf{B}_P \cdot \nabla)\Omega$ (where ρ is the cylindrical radial coordinate, \mathbf{B}_P the poloidal magnetic field, ∇ the differential operator and Ω the rotation rate) is symmetric about the mid plane. Following such an argument, an analytical expression was obtained for the final toroidal field at the asymptotic radial limit for a given constant of diffusion. Mestel (1999) explained the need for toroidal currents to maintain the poloidal fields and *vice versa* in the interiors of stars and presented a wave equation for the rotation rate. Spruit (1999) discussed the interplay between differential rotation and magnetic fields in stellar interiors, focusing on the inherent instabilities that may occur in such systems.

These works have largely been based on analytical results or analytical extensions of the kinematic dynamo equations. There is a need to confirm and extend these results using realistic magneto–hydrodynamic simulations. However, such numerical computations have been difficult due to the inherent non–deterministic nature of the problem and due to the several numerical instabilities that can occur during the simulation. Only recently have reliable and stable numerical schemes been formulated and initial steps towards realistic simulations of these systems been undertaken. Shapiro (2000) solved the incompressible, non–turbulent, non–diffusive hydromagnetic dynamo equations both analytically and numerically and showed that for assumed seed magnetic fields, viscosity effectively brakes differential rotation. It was also shown that an infinite cylindrical star, with an impressed internal monopolar field, can lose angular momentum to an external plasma medium, even in the absence of viscosity. The effects of compressibility was discussed by Cook, Shapiro & Stephens (2003) who showed that radial flow and shocks become important in the evolution. Liu & Shapiro (2004) worked out these effects for relativistic spherical stars with quadrupolar and dipolar internal fields.

Considering, the complexities involved in these simulations and the high potential for these techniques to be used to understand the dynamic behavior of neutron stars and other astrophysical systems, it is prudent to develop different numerical schemes to cross verify the results obtained. Moreover, having different reliable schemes gives the flexibility to choose the one which can be most easily adapted for a particular application. By far, the best advantage is of obtaining different physical insight when the problem is solved for different settings.

In this work, we present and implement a numerical magneto–hydrodynamic scheme to study the dynamics of differentially rotating proto–neutron stars. Assuming the proto–neutron star to be composed of an incompressible homogeneous fluid, we evolve the toroidal components of the magnetic field and flow for fixed poloidal components. The star is assumed to be spherical in shape and the kinetic energy of rotation is assumed to be far lesser than the magnetic energy which itself is far lesser than the gravitational energy. The scheme is tested against numerical dissipation of physically conserved quantities and verified by comparing the results obtained with those from similar numerical computations (Liu & Shapiro 2004). Although the model used to represent the proto–neutron star is simplistic, we show that qualitative insights on the dynamic behavior of such systems can be obtained. The motivation here is to present a reliable numerical scheme which may be further developed to simulate realistic neutron stars and other astrophysical systems.

In the next section (2) the details of the technique are presented. In section(3) the results of the simulations are given which are discussed in section (4). Appendix A provides the details of numerical implementation of the equations.

2. Methodology

We assume the differentially rotating star to be made up of a homogeneous, incompressible, perfectly conducting fluid. The relevant Magnetohydrodynamic (MHD) equations are:

$$\nabla \cdot \mathbf{v} = 0 \tag{1}$$

$$\frac{\partial \mathbf{v}}{\partial t} + (\mathbf{v} \cdot \nabla) \mathbf{v} = -\frac{1}{\epsilon} \nabla P - \nabla \Phi + \nu \nabla^2 \mathbf{v} + \frac{(\nabla \times \mathbf{B}) \times \mathbf{B}}{4\pi\epsilon} \quad (2)$$

$$\nabla^2 \Phi = 4\pi G \epsilon \quad (3)$$

$$\nabla \cdot \mathbf{B} = 0 \quad (4)$$

$$\frac{\partial \mathbf{B}}{\partial t} = \nabla \times (\mathbf{v} \times \mathbf{B}) \quad (5)$$

where \mathbf{v} is the fluid velocity, P the material pressure, ϵ the matter density, Φ the gravitational potential, ν the kinematic viscosity and \mathbf{B} the magnetic field.

For our purpose here, we assume the star to be spherically symmetric (with a radius R) and immersed in an ambient plasma. The initial differential rotation is taken to be constant along cylinders, and the poloidal component of the internal magnetic field to be time-independent and given to be a pure dipole:

$$B^\rho(t, \rho, z) = \frac{\mu}{R^3} \frac{3\rho z}{(\rho^2 + z^2)^{5/2}} \quad (6)$$

$$B^z(t, \rho, z) = \frac{\mu}{R^3} \frac{(2z^2 - \rho^2)}{(\rho^2 + z^2)^{5/2}}$$

where μ is the magnetic moment. We make use of cylindrical coordinates: ρ, z (scaled with respect to R) and φ here (the spherical symmetry of the star notwithstanding, the quantities that are being considered in this problem possess axial symmetry in general). Such a magnetic field being divergence and curl free, nonetheless, represents a field in vacuum (rather than one that resides inside a medium as is considered here) and contains a singularity at the centre. Since this field is time-independent, and we assume a purely axial flow, the central singularity in the magnetic field does not induce irregular behaviour in the velocity field (even though in the final state, the rotation rate will have a singularity at the centre) or the azimuthal magnetic field. In the event of performing more realistic calculations, with more realistic magnetic field structures (such as the output of gravitational collapse codes), the numerical techniques developed here for treating such a restrictive magnetic field structure (the central singularity turns up as a stringent Courant condition) is expected to prove handy.

In order to compare with previous calculations in the literature, we use the same initial rotational and toroidal magnetic field profiles as that of Shapiro (2000), viz.:

$$\Omega(0, \rho, z) = \frac{1}{2} \Omega_0 [1 + \cos(\pi \rho^2)] \quad (7)$$

$$B^\varphi(0, \rho, z) = 0 \quad (8)$$

$$(9)$$

where Ω_0 represents a characteristic rotation rate at the centre.

For our assumptions to be self consistent, we require $T \ll \mathcal{M} \ll W$, where T is the rotational kinetic energy, \mathcal{M} , the total magnetic energy and W the gravitational potential energy. In other words, for the magnetic field structure that we assume here, at time $t > 0$

$$(B^\rho)^2 + (B^z)^2 \gg (B^\varphi)^2 \sim 4\pi\epsilon\rho^2\Omega^2$$

Since there is no mass in-flow to the system and since the system is homogeneous the poloidal equations decouple from the toroidal component of the Navier–Stokes equation (Shapiro & Teukolsky 1983). We also assume that viscous dissipation, turbulence, convection and diffusion are absent in the system. Another tacit assumption is that the system is stable against the innumerable plasma/MHD instabilities (Spruit 1999).

2.1. Flow and Magnetic Field Parameters

2.1.1. Formalism

For our treatment here, we make use of the natural coordinates available to us, viz., one that follows the magnetic field lines. For the sake of comparison with the equivalent 1–D problem, we use a modified version of magnetic flux coordinates by defining the magnetic field as

$$\mathbf{B} = \nabla\psi \times \nabla\varphi \quad (10)$$

To be consistent with our assumptions of the time independent poloidal field dominating over the time dependent toroidal field, the equality above is only approximate. With such a definition, we further choose

$$\hat{\psi} = \psi/(\mu R) = \frac{\rho^2}{(\rho^2 + z^2)^{3/2}} \quad (11)$$

$$\hat{\varphi} = \varphi \quad (12)$$

$$\rho = \rho \quad (13)$$

to be the first, second and third coordinate respectively. These choices are such that $\hat{\psi}$ is constant along a magnetic field line. The inverse transformations are:

$$z = \sqrt{\left(\frac{\rho^2}{\hat{\psi}}\right)^{2/3} - \rho^2} \quad (14)$$

$$\varphi = \hat{\varphi} \quad (15)$$

$$\rho = \rho \quad (16)$$

In the following paragraphs, we drop the ‘carets’ from the variables and tacitly understand the variables to be dimensionless. With this, treatment, we have for the new coordinate system

$$\mathbf{B} = (B^\psi, 0, B^\rho) \quad (17)$$

$$B^\psi = 0 \quad (18)$$

$$h_\psi = \sqrt{g_{\psi\psi}} = 1/(\rho B^\rho) \quad (19)$$

$$h_\varphi = \sqrt{g_{\varphi\varphi}} = \rho \quad (20)$$

$$h_\rho = \sqrt{g_{\rho\rho}} = B/B^\rho \quad (21)$$

$$g_{\psi\rho} = B^z/(\rho(B^\rho)^2) \quad (22)$$

$$g_{\psi\varphi} = 0 = g_{\rho\varphi} \quad (23)$$

$$g = g_{\varphi\varphi}(g_{\psi\psi}g_{\rho\rho} - g_{\psi\rho}^2) = 1/(B^\rho)^2 \quad (24)$$

we have again, as earlier, made the tacit assumption of neglecting the B^φ in comparison to the poloidal components. In the above equations, $B = \sqrt{(B^\rho)^2 + (B^z)^2}$ is the magnitude of the magnetic field, g_{ij} and h_i (with $i, j = \psi, \varphi, \rho$) are the metric coefficients and scale factors respectively and g is the determinant of the metric tensor. On a single field line, the metric reduces to:

$$d\hat{s} = h_\rho d\rho \quad (25)$$

where \hat{s} is the length along the magnetic field line. Equation (25) agrees with the equation of a magnetic field line (D’haeseleer et al. 1991). Integrating this last equation gives the length of the magnetic field line $\hat{s}_{\max}(\psi)$.

In this new coordinate system, the azimuthal components of the Navier Stokes and magnetic induction equations reduce to:

$$\frac{\partial v^\varphi}{\partial t} = \frac{1}{4\pi\epsilon} \frac{h_\psi B^\rho h_\rho}{\sqrt{g} \hat{s}_{\max}(\psi)} \frac{\partial}{\partial s} (h_\varphi B^\varphi) \quad (26)$$

$$\frac{\partial B^\varphi}{\partial t} = \frac{h_\varphi h_\rho}{\sqrt{g} \hat{s}_{\max}(\psi)} \frac{\partial}{\partial s} (h_\psi v^\varphi B^\rho) \quad (27)$$

where we denote $s = \hat{s}/\hat{s}_{\max}(\psi)$. These are the counterparts of the 2-D equations (in cylindrical coordinates) given below:

$$\frac{\partial v^\varphi}{\partial t} = + \frac{1}{4\pi\epsilon} \left[\frac{B^\rho}{R\rho} \frac{\partial}{\partial \rho} (\rho B^\varphi) + \frac{B^z}{R\rho} \frac{\partial}{\partial z} (\rho B^\varphi) \right] \quad (28)$$

$$\frac{\partial B^\varphi}{\partial t} = \frac{1}{R} \left[\frac{\partial}{\partial z} (v^\varphi B^z) + \frac{\partial}{\partial \rho} (v^\varphi B^\rho) \right] \quad (29)$$

2.1.2. Computational Domain

The central singularity in the magnetic field now shifts to a coordinate singularity for ψ . Numerically, we take care of this singularity by introducing a new variable q such that $\psi = q/(1 - q)$. We make another numerically convenient

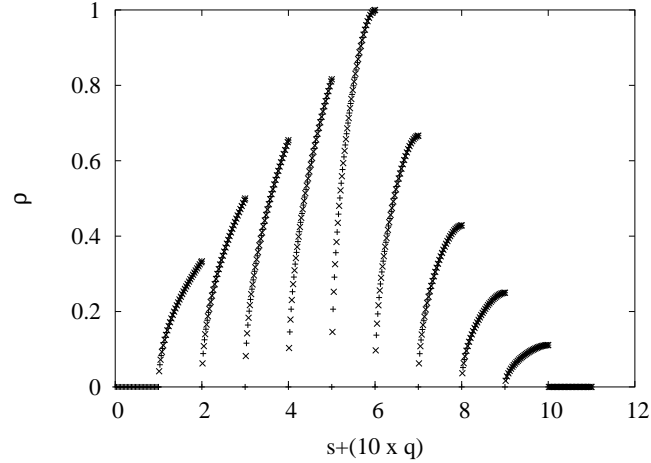


Fig. 1. The variation of ρ with respect to $s + (10 \times q)$ for a dipolar magnetic field. This and other figures (unless explicitly mentioned) employ 11 values of q ; each value corresponding to a field line. For each line, the value of q can be read off from the x-axis of this figure (since $0 < s < 1$ as $0 < \rho < \rho_{\max}$, where ρ_{\max} corresponds to the value of the cylindrical radial coordinate at the surface of the star). The lowest value of q corresponds to an ‘open’ field line almost parallel to the rotation axis while the largest one corresponds to a ‘closed’ field line enclosing the core of the star. The line corresponding to $q = 0.5$ is the marginally ‘closed’ field line intersecting the equator at the surface of the star. Predictably, the non-linearity of the variation increases with q .

change of variable by integrating Eq. (25) to obtain the length of the magnetic field line (\hat{s}_{\max}) and then scaling the variable \hat{s} with this quantity to obtain a new coordinate $s = \hat{s}/\hat{s}_{\max}$. In Fig. 1 we display the result of such an integration and plot ρ with $s + 10 \times q$ for the dipolar magnetic field. With these change of variables, the two independent spatial coordinates in the system of equations are q , and s such that $0 < q < 1$ and $0 < s < 1$. We have therefore, converted the curved field lines into straight field lines as shown in the left panel of Fig. 2. The projected field lines

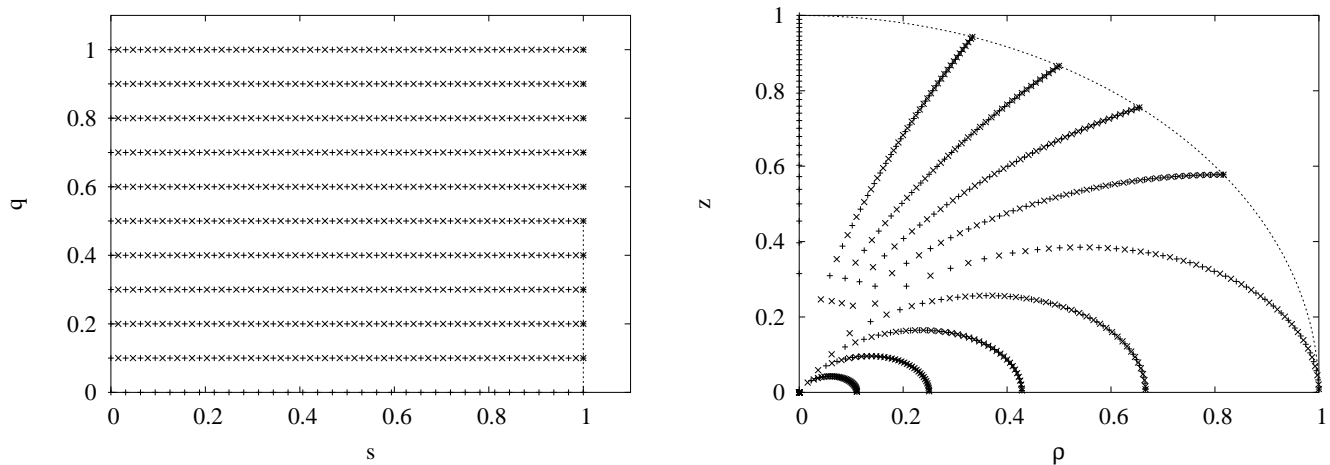


Fig. 2. Computational domain: in the left panel are the field lines depicted by the ‘crosses’ and the ‘pluses’ for q v/s s ; the vertical line represents the surface of the star (the region $q > 0.5$ represents the ‘closed’ field line that never intersect the stellar surface), the right panel displays the grid points projected onto the field lines in real space (cylindrical coordinates z v/s ρ) - the coordinate q labels each of these lines. The ‘crosses’ correspond to ‘cell boundaries’ at which B^φ is defined, while the ‘pluses’ correspond to ‘cell centres’ where Ω is defined in the staggered space scheme that we use here.

with the grid points are shown in Fig. 2, right panel. Since the relationship between z and ψ is non-linear such that z blows up for low ψ values, the central points for these values of ψ look sparse in Fig. 2 right panel.

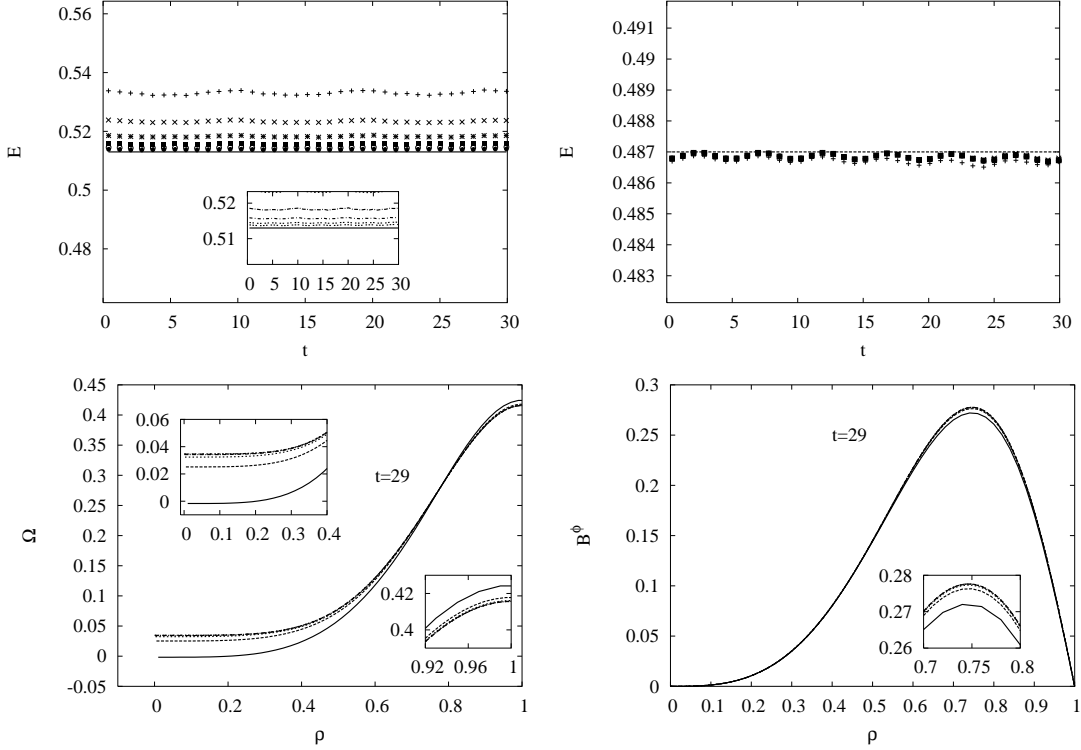


Fig. 3. Convergence tests: For the monopolar field case, for vacuum exterior. Top left panel is the convergence test for the minimum value of E_{rot} : the straight line corresponding to 0.513 is the analytically expected value; the limits on the y-axis represent 10% variation from this value, the ‘+’ are the numerically obtained values with 51 grid points, the ‘x’ with 101 grid points, the ‘*’ with 201, the filled squares with 401, the empty circles with 801 and the filled circles with 1601 (the last three appear merged in the main figure). The inset shows a blown up view of the same: solid line remains the same, the dashed line is with 101, the long dash-dot line with 201, the medium dash-dot line with 401, the short dash-dot line with 801 and the dot-dot-dashed line with 1601 grid points respectively. The top right panel is the maximum value of E_{mag} , the analytically expected value of 0.487 is represented by the straight line; the limits of the y-axis correspond to a 1% variation. The numerically obtained values for these are fairly well covered even for 50 grid point resolution. The bottom left panel is the Ω profile at a late time of $t = 29$. The curves have the same meaning as for the E_{rot} convergence. The bottom right panel displays the B^φ profile at $t = 29$.

2.1.3. Initial and Boundary Conditions

We assume that the differential rotation is zero at the center. This amounts to saying that:

$$\left. \frac{\partial \Omega}{\partial s} \right|_{(t,q,s=0)} = 0 \tag{30}$$

$$\left. \frac{\partial B^\varphi}{\partial t} \right|_{(t,q,s=0)} = 0 \tag{31}$$

For the outer boundary conditions, let us first consider the ‘closed’ field lines. From symmetry about the equator, we know that all the derivatives in the vertical direction vanish in the equatorial plane, in addition $B^\rho = 0$ in the equatorial plane. From Eq. (29) we see therefore that at $s = 1$

$$B^\varphi(t, q, s = 1) = 0 \tag{32}$$

For the ‘open’ field lines, in a similar manner to Shapiro (2000), we can show using Roberts (1968) that for our straight field lines

$$\left. \frac{\partial B^\varphi}{\partial t} \right]_{(t,q,1)} + \left. \frac{\partial B^\varphi}{\partial s} \right]_{(t,q,1)} v_A \frac{(1+\mathcal{R})}{(1-\mathcal{R})} = 0 \quad (33)$$

where \mathcal{R} is the reflection coefficient for the azimuthal magnetic field amplitude:

$$\mathcal{R} = \frac{\sqrt{(\epsilon_{\text{ex}}/\epsilon)} - 1}{\sqrt{(\epsilon_{\text{ex}}/\epsilon)} + 1} \quad (34)$$

and $v_A = B_0/\sqrt{4\pi\epsilon}$ is the surface Alfvén speed with $B_0 = \mu/[h_\varphi]^3$ being the representative surface magnetic field. It must be noted here that the actual internal Alfvén speed, $v_A^0 = B(\rho=0, z=0)/\sqrt{4\pi\epsilon} \gg v_A$.

For the initial conditions, as mentioned earlier, we assume that $\Omega(0, q, s)$ is given by equation (9). We also assume the toroidal magnetic fields to be absent to begin with i.e. $B^\varphi(0, q, s) = 0$.

2.1.4. Non-Dimensional Formulation

For the sake of numerical convenience, we scale the dimensions out of the equations through the following identifications:

$$\begin{aligned} h_\varphi &= [h_\varphi] \hat{h}_\varphi, & h_\psi &= [h_\psi] \hat{h}_\psi, & h_\rho &= [h_\rho] \hat{h}_\rho, & g &= [g] \hat{g}, & v^\varphi &= [h_\varphi] \Omega, \\ \Omega &= \Omega_0 \hat{\Omega}, & B^\rho &= B_0 \hat{B}^\rho, & B^\varphi &= \sqrt{4\pi\epsilon} \Omega_0 [h_\varphi] \hat{B}^\varphi, & t &= 2\hat{t}/([h_\varphi]/v_A), & \frac{[h_\varphi][h_\psi][h_\rho]}{\sqrt{[g]}} &= 1, \\ E &= \left(\frac{4\pi}{3} \epsilon \frac{\sqrt{[g]}\psi[h_\varphi]}{[h_\rho]} \right) \frac{[h_\varphi]^2 \Omega_0^2}{2} \hat{E}, \\ J &= \left(\frac{4\pi}{3} \epsilon \frac{\sqrt{[g]}\psi[h_\varphi]}{[h_\rho]} \right) [h_\varphi] \rho^2 \Omega_0 \hat{J} \end{aligned}$$

2.1.5. Evolution Equations

The non-dimensional form of the evolution Eqs. (26) and (27) become:

$$\frac{\partial \hat{\Omega}}{\partial \hat{t}} = \frac{\hat{h}_\psi \hat{B}^\rho \hat{h}_\rho}{2\hat{h}_\varphi \sqrt{\hat{g}} s_{\text{max}}(q)} \frac{\partial}{\partial s} (\hat{h}_\varphi \hat{B}^\varphi) \quad (35)$$

$$\frac{\partial \hat{B}^\varphi}{\partial \hat{t}} = \frac{\hat{h}_\varphi \hat{h}_\rho}{2\sqrt{\hat{g}} s_{\text{max}}(q)} \frac{\partial}{\partial s} (\hat{h}_\psi \hat{h}_\varphi \hat{\Omega} \hat{B}^\rho) \quad (36)$$

where we have identified v^φ with $h_\varphi \Omega$.

2.1.6. Energy and Angular Momentum Conservation

As energy conservation acts as a check to the numerical computations, we compute the relevant energies in the system. In the non-dimensional units, the integrals for rotational kinetic energy, toroidal magnetic energy and Poynting energy are given as (in the equations below, $d\tau$ represents the volume element in cylindrical coordinates):

$$\mathcal{E}_{\text{rot}}(t) = \int d\tau (\epsilon \Omega(t, \rho, z)^2 \rho^2 / 2) = \int d\hat{\psi} \hat{E}_{\text{rot}} \quad (37)$$

$$\mathcal{E}_{\text{mag}}(t) = \int d\tau [(B^\varphi(t, \rho, z))^2 / 8\pi] = \int d\hat{\psi} \hat{E}_{\text{mag}} \quad (38)$$

$$\begin{aligned} \mathcal{E}_{\text{Poy}}(t) &= \int_0^t dt \dot{\mathcal{E}}_{\text{Poy}}(t) = - \int_0^t dt \left(\int_{\hat{s}=\hat{s}_{\text{max}}} h_\psi h_\varphi d\psi d\varphi \frac{B^\varphi B^\rho \Omega h_\varphi}{4\pi} \right) = - \int_0^t dt \left(\int d\hat{\psi} \hat{\mathcal{E}}_{\text{Poy}} \right)_{\hat{s}=\hat{s}_{\text{max}}} \\ &= \int d\hat{\psi} \hat{E}_{\text{Poy}} \end{aligned} \quad (39)$$

where $\hat{\mathcal{E}}_{\text{Poy}} = -\frac{1}{2}h_\varphi B^\varphi \Omega$ and

$$\hat{E}_{\text{rot}} = \frac{3}{2} \int ds \sqrt{\hat{g}} \frac{\hat{s}_{\text{max}}}{\hat{h}_\rho} \hat{h}_\varphi^2 \hat{\Omega}^2 \quad (40)$$

$$\hat{E}_{\text{mag}} = \frac{3}{2} \int ds \sqrt{\hat{g}} \frac{\hat{s}_{\text{max}}}{\hat{h}_\rho} (\hat{B}^\varphi)^2 \quad (41)$$

$$\hat{E}_{\text{Poy}} = -\frac{3}{2} \int_0^{\hat{t}} dt \left(\hat{B}^\varphi \hat{\Omega} \hat{h}_\varphi \right)_{\hat{s}=\hat{s}_{\text{max}}} \quad (42)$$

are the energies associated with a given magnetic field line. Conservation of energy requires

$$\mathcal{E}_{\text{rot}}(0) = \mathcal{E}_{\text{rot}}(t) + \mathcal{E}_{\text{mag}}(t) + \mathcal{E}_{\text{Poy}} \quad (43)$$

However, it may be noted that Eq. (43) is satisfied if on each magnetic field line:

$$\hat{E}_{\text{rot}}(0) = \hat{E}_{\text{rot}}(t) + \hat{E}_{\text{mag}}(t) + \hat{E}_{\text{Poy}}(t) \quad (44)$$

holds.

The angular momenta integrals are:

$$\mathcal{J}_{\text{rot}}(t) = \int d\tau (\epsilon \Omega(t, \rho, z) \rho^2) = \int d\hat{\psi} \hat{J}_{\text{rot}} \quad (45)$$

$$\mathcal{J}_{\text{mag}}(t) = \int_0^t dt \mathcal{N} = \int d\hat{\psi} \hat{J}_{\text{mag}} \quad (46)$$

where $\mathcal{N} = \hat{\mathcal{E}}_{\text{Poy}}/\Omega$ is the torque exerted by the Maxwell stress at the surface and

$$\hat{J}_{\text{rot}} = \frac{3}{2} \int ds \sqrt{\hat{g}} \frac{\hat{s}_{\text{max}}}{\hat{h}_\rho} \hat{h}_\varphi^2 \hat{\Omega} \quad (47)$$

$$\hat{J}_{\text{mag}} = -\frac{3}{4} \int_0^{\hat{t}} dt \left(\hat{B}^\varphi \hat{h}_\varphi \right)_{\hat{s}=\hat{s}_{\text{max}}} \quad (48)$$

2.2. Numerical Scheme

Since the coefficients to the differentials in Eqs. (35) and (36) depend on some powers (> 1) of inverse of the coordinate distance from the centre, clearly, a fully explicit scheme may prove to be highly restrictive due to the Courant condition. For the equivalent 1-D problem, it was shown (Shapiro 2000) that for a fully implicit scheme employing a 2nd order staggered space and 1st order time, the Courant condition only proves to be a restriction for accuracy (numerical stability being assured) – and the energy conservation (and angular momentum conservation in the case of energy dissipation due to an external plasma) is the marker for the accuracy. Accordingly, for our purpose here we use a staggered leapfrog scheme. The recipe for the finite differencing for such a scheme is mentioned in the Appendix.

The details on the numerical checks performed on the code *vis-á-vis* the one-dimensional formalism of Shapiro (2000) is provided in section (3) below.

3. Results

In this paper, we calculate the timescales of the damping of differential rotation by magnetic fields. We have assumed a spherically symmetric star, having an applied (by hand) internal dipole magnetic field (that is divergence free everywhere and, in addition curl free everywhere except the centre). The initial differential rotation law is chosen (Shapiro 2000) to be given by Eq.(9) and initially, toroidal magnetic fields are assumed to be absent. For such a magnetic field configuration and initial rotation law, we solve the azimuthal components of the Navier–Stokes' equation and the Maxwell magnetic induction equation. For computational and physical convenience, we choose to solve these equations in a modified Magnetic Flux Co-ordinate system. This facilitates us to solve a series of 1-D equations, parametrised by a stream function. Using a staggered Leap-frog scheme, we difference the system of equations (as mentioned in Appendix) on a uniform q and s grid. In this section, we provide the results of our computations. For illustrative purposes, we have considered only 11 field lines (consistent with Figs. 1 and 2) and display results for 3 field lines; in addition, we also display results for the surface and the equator (essentially one point for each field line) – for these, we have had to use 201 field lines for the purpose of clarity in the dynamics.

3.1. Checks on the code: simulations for a monopole field configuration

We first checked the code for a satisfactory reproduction of the 1–D results reported in Shapiro (2000). A trivial identification of $(\psi \rightarrow z, \varphi \rightarrow \varphi, \rho \rightarrow \rho)$ gives us the monopolar magnetic field. In the above identification, the azimuthal Eqs. (26) and (27) reduce to those in Shapiro (2000) and as is mentioned therein, the energy conservation is an indicator of the accuracy of the numerical scheme. In Fig. 3 we display the convergence tests for the vacuum exterior case using resolutions corresponding to 51, 101, 201, 401, 801 and 1601 grid points on a single magnetic field line. The top left panel has the minimum values of E_{rot} (scaled to the value of the initial E_{rot}). The straight line located at 0.513 is the analytically obtained value for this quantity. The upper and lower limit on the y -axis correspond to a 10% variation from this mean value. The top right panel displays the maximum value for the variations in E_{mag} (again scaled to the initial E_{rot}). The analytical estimate of 0.487 is represented by the straight line located at the mid-point of the y -axis in the plot displaying a maximum variation of 1% in the limits. The bottom left panel displays the Ω profile at time $t = 29$ a time where energy deviates substantially for the lowest resolution of 51 points. Understandably (from Eq. 40), the corresponding deviations in Ω from the high resolution case is less significant than for E_{rot} . The bottom right panel displays the B^φ profile at $t = 29$. The ratio of the exterior density to the interior: $\epsilon_{\text{ex}}/\epsilon = 0.2$.

3.2. Simulations for the dipole field configuration

We discuss the results for three field lines: one that is ‘open’ another that is ‘closed’ and yet another that is ‘marginally closed’ which we term *equatorial*, the latter two differing from the former through the boundary conditions as explained in section (2.1.3) and easily deduced from Fig. 2. In particular out of the 11 field lines that we consider here, we discuss the results for $q = 0.3$ (open), $q = 0.6$ (closed) and $q = 0.8$ (closed).

3.2.1. Results for the open field line ($q = 0.3$)

The dynamics of the variation of the rotation and the toroidal magnetic field are as shown in Fig. 5. We have used 851 points along the field line direction. As can be seen, the torque between the stellar surface and the ambient plasma take away angular momentum from the star so that the rotation rate along the field line becomes uniform (Fig. 5 lower panel). A plot of the energy and angular momentum variation over the dimensionless time t is depicted in Fig. 6. Unlike for the monopolar case, the assumed ratio of density does not lead to retrograde rotation – this is because the curvature of the magnetic field line produces a lesser torque.

3.2.2. Results for the closed field line ($q = 0.6$)

The dynamics of the variation of the rotation and the toroidal magnetic field are as shown in Fig. 7. For this field line, we have used 1401 points in the line direction. Since this is a ‘closed’ field line and there is no dissipation in the system, the oscillations are sustained. At late times, the toroidal magnetic field profiles develop high gradients at the surface. This is due to $\partial\Omega/\partial s$ not remaining zero at the surface at later times (as a result of the singularity of $\partial z/\partial\rho$ at the equator). The energy conservation, however, still holds (the small variation from conserved value is due to the truncation error induced due to insufficient grid points). A key difference in the energy variation is the existence of a low frequency component (in comparison with the 1–D counterpart) – this difference is due to the fact that in the 1–D case, the substitution of the induction equation into the Navier–Stokes equation yields a wave equation (Shapiro 2000) in cylindrical coordinates, however, in our general form, such a substitution results in a wave equation with an advective component. The low frequency component in the energy variation with time, represents the oscillation of the point of inflection in our differential rotation law due to this advection.

3.2.3. Results for the closed field line ($q = 0.8$)

The dynamics (as earlier) is depicted in Fig. 9. The energy variation with time is shown in Fig. 10. We have used 851 data points. The deviation of the total energy for the value of 1 is due to truncation errors.

3.3. Variation of Ω and B^φ at the surface

We have seen from Figs. 5, 7 and 9 that the dynamics of magnetic field and rotation rate variation with time along a given field line is smooth. However, if we use real (spherical/cylindrical) coordinates, the picture is different – since the oscillation along a field line is uncorrelated with that of an immediate neighbour, beyond a certain time, the oscillations get out of phase as can be seen in Fig. 11 along the surface of the star. Structures form, however since Poynting flux is carried away from the star, these settle down at late times to equilibrium values in off-equatorial regions. Since at

the equator, there are no toroidal magnetic fields generated, the oscillation is perpetual (unless diffusion or dissipation comes into play) – this fact, therefore, underlines the importance of taking into account diffusion to realistically model the system (Spruit 1999, Liu & Shapiro 2004).

3.4. Variation of Ω in the equatorial plane

Fig. 12 illustrates the dynamical behaviour along the equator. The structures keep building up at late times here and it is important to consider diffusion or viscous dissipation so that the neighbouring lines ‘talk’ to each other.

4. Discussion

We have computed the dynamical evolution of rotation and toroidal magnetic fields for a spherical star composed of an incompressible homogeneous, differentially rotating fluid having an internal time independent dipolar magnetic field. Given these assumption one can expect the following physical processes to take place: At time $t = 0$, within the spherically symmetric differentially rotating star, a dipolar magnetic field is switched on. From Ferraro (1937) law of isorotation, we know that the lowest energy state of the system is when the rotation rate is constant along the magnetic field lines (provided there is dissipation in the system). For this to happen, the fluid pulls the poloidal magnetic field lines, producing toroidal magnetic fields. In turn the toroidal magnetic field acts back on the plasma. In the absence of losses from the system, this leads to sustained oscillations. For an internal dipolar magnetic field, exchange between rotational and toroidal magnetic field energies will take place along the ‘closed’ field lines (fig) at characteristic frequencies. Along the open field lines, on the other hand, there will exist non-zero toroidal surface magnetic fields, that will be radiated away (or go into spinning up the ambient plasma) leading to losses from the system. This implies that after several Alfvén time-scales, Ferraro law of isorotation will hold on the open field lines.

We have shown here that for the ‘open’ field lines, rigid rotation is achieved (in accordance with Ferraro’s law) through the loss of Poynting flux to an ambient plasma, while the ‘closed’ field line execute torsional oscillation through backreaction between toroidal magnetic and rotational kinetic energies.

Although a first glance at Eq. 27 indicates that the right hand side becomes ∞ at the centre, it can be seen from a more careful observation and the acknowledgement of the fact that these equations are for a given magnetic field line, that the quantity within parenthesis will be Ω and from our boundary conditions $\partial\Omega/\partial s$ becomes zero at the centre. The upshot of this is that for different field lines, Ω possesses different values at the centre – a manifestation of the singularity in the poloidal magnetic field and ψ .

An important result (and verification of the results of Liu & Shapiro 2004) is the relative difference in phases of oscillation of nearby points at 2–3 Alfvén timescales when one samples a radial or polar zone (Figs. 11 and 12): implying large phase deviation at late times (Spruit 1999). Such a behaviour is a result of our restrictive assumptions of neglecting diffusion and evolution of the poloidal field. Another point that the figures emphasise is the probable inefficacy of using pure spherical or cylindrical coordinates for analysing the dynamics of such a system in the absence of viscosity.

The simplistic assumption of an internal dipolar magnetic field with ‘closed’ field lines is used as an illustrative example – the high restrictiveness of the sustenance of oscillation in such a system tests the efficacy of the code and the formalism in general. Hence, for the purposes of this paper, the origin and sustenance of such a field in matter is taken for granted. The formalism and the code amply demonstrate tenacity while the veracity of the numbers is ignored over obtaining the qualitative behaviour. The key aspect of the dynamics (when there is dissipation and according to Ferraro’s law) is that it is all about matching two functions (through dissipation and readjustment of the angular momentum in the system): one that is constant along cylinders (the initial differential rotation rate) to another that follows the dipolar field.

The evolution of the collapsing core of the progenitor star to pulsars is characterised by strong convection and turbulence. The convection is driven by neutrino transport and ceases when the star becomes transparent to neutrinos – an α - ω dynamo operates in this regime (Thompson & Duncan 1993; Duncan & Thompson 1992) amplifying the primordial magnetic fields to saturation levels $B_{\text{sat}} \sim 10^{14}$ G. We dynamically place our system at a point after the cessation of convection and with a predominantly poloidal nature to the magnetic field – i.e. at about $t \gtrsim 30$ s after collapse. The next leg in the journey to computing equilibrium models of rotating magnetised stars will be the incorporation of less restrictive magnetic field geometries and the effects of dissipation.

Acknowledgements. The author thanks H.M. Antia and Kandaswamy Subramaniam for discussions. Thanks are also due to Bobo Ahmedov, Ranjeev Misra, Koji Uryu, and Shin Yoshida, for a critical reading of the manuscript and stimulating discussions. Luciano Rezzolla and John Miller are thanked for their suggestion of this project. This work was supported by visiting fellowships at TIFR and IUCAA. The author thanks Alak Ray, Ajit Kembhavi and the deans and directors of TIFR and IUCAA for kind hospitality. The computations were performed on the “Compaq Tru 64” clusters at TIFR and IUCAA computer centres.

Appendix A: Numerical Scheme

In this section we describe the numerical scheme that we employ. The equations that we solve are of the type:

$$\frac{\partial X}{\partial t} = \mathcal{A} \frac{\partial}{\partial s} (\mathcal{B}Y) \quad (\text{A.1})$$

$$\frac{\partial Y}{\partial t} = \mathcal{C} \frac{\partial}{\partial s} (\mathcal{D}X) \quad (\text{A.2})$$

We assume X and Y to be functions of t , s and q (dependence on q is implicit as the eqns. (A.1) and (A.2) are for constant values q). When we finite difference the above equations, we define X and Y on alternate grid points so as to yield a staggered mesh (and hence a second order treatment for space). Typically, we demand that X be defined on ‘half’ grid points (cell boundaries) and Y on ‘full’ grid points (cell centres). Accordingly, the dependent variables will carry the tag:

$$X(t, s, q) = X_{i+1/2, j}^n, X_{i+3/2, j}^n \dots (i \in [1, N-1]) \quad (\text{A.3})$$

$$Y(t, s, q) = Y_{i, j}^n, Y_{i+1, j}^n \dots (i \in [1, N]) \quad (\text{A.4})$$

where N is the total no. of grid points along a given magnetic field line (i.e. a given q). Since we’re working on constant q (and hence constant j) lines, for the sake of easy representation here, we shall drop the subscript j from the variables (nevertheless remembering that the variables are indeed three dimensional). Thus, for a given q :

$$X(t, s) = X_{i+1/2}^n, X_{i+3/2}^n \dots (i \in [1, N-1]) \quad (\text{A.5})$$

$$Y(t, s) = Y_i^n, Y_{i+1}^n \dots (i \in [1, N]) \quad (\text{A.6})$$

We discretise Eqs. (A.1) and (A.2) in staggered leap–frog scheme as mentioned below:

$$\frac{X_{i+1/2}^{n+1} - X_{i+1/2}^n}{\Delta t} = \mathcal{A}_{i+1/2} \left(\frac{\mathcal{B}_{i+1} Y_{i+1}^n - \mathcal{B}_i Y_i^n}{\Delta s} \right) \quad (\text{A.7})$$

$$\frac{Y_i^{n+1} - Y_i^n}{\Delta t} = \mathcal{C}_i \left(\frac{\mathcal{D}_{i+1/2} X_{i+1/2}^n - \mathcal{D}_{i-1/2} X_{i-1/2}^n}{\Delta s} \right) \quad (\text{A.8})$$

References

- Andersson, N. 2003, CQGGr, 20, 105
 Arras, P., Flanagan, E.E., Morsink, S.M., Schenk, A.K., Teukolsky, S.A., Wasserman, I. (2003), ApJ, 591, 1129
 Bhattacharya, D. & van den Heuvel, E.P.J. 1991, Phys. Reports, 203, 1
 Bhattacharya, D. 2002, J. Astrophys. & Astronomy, 23, 67
 Blandford, R.D., Applegate, J.H., & Hernquist, L. (1983), MNRAS, 204, 1025
 Chanmugam, G., Rajasekhar, A., & Young, E.J. MNRAS, 276, L21
 Cook, J.N., Shapiro, S.L., Stephens, B.C. (2003), ApJ, 599, 1272
 D’haeseleer, W.D., Hitchon, W.N.G., Callen, J.D., Shohet, J.L. (1991), *Flux coordinates and magnetic field structure*, (Berlin: Springer–Verlag)
 Duncan, R. C., & Thompson, C. 1992, ApJ, 392, L9
 Ferraro, V.C.A. (1937), MNRAS, 97, 458
 Geppert, U. & Urpin, V. (1994), MNRAS, 271, 490
 Gil, J. & Mitra, D. (2001), ApJ, 550, 383
 Heger, A., Woosley, S.E., Langer, N., & Spruit, H.C. 2003, IAU Symp. 215, (astro-ph/0301374)
 Jones, P.B. 2001, Phys. Rev. Lett., 86, 1384
 Konar, S. & Bhattacharya, D. (1997), MNRAS, 284, 311
 Konar, S. & Bhattacharya, D. (1999), MNRAS, 303, 588
 Lindblom, L., Owen, B.J., Morsink, S.M. 1998, Phys. Rev. Lett., 80, 4843
 Liu, Y.T. & Shapiro, S.L. (2004), Phys Rev D, 69, 044009
 Mestel, L. 1999, *Stellar Magnetism* (Oxford: Clarendon Press)
 Mitra, D., Konar, S., & Bhattacharya, D. (1999), MNRAS, 307, 459
 Moffat, H. K. 1978, *Magnetic Field Generation in Electrically Conducting Fluids* (Cambridge: Cambridge Univ. Press)
 Rampp, M., Muller, E., & Ruffert, M. 1998, A&A, 332, 969
 Rasio, F.A. & Shapiro, S.L. (1999), Class. Quant. Grav., 16, R1
 Rezzolla, L., Lamb, F.K., & Shapiro, S.L. 2000, ApJ, 531, L139
 Rezzolla, L., Lamb, F.K., Markovic, D., & Shapiro, S.L. (2001), Phys. Rev. D, 64, 104013

- Rezzolla, L., Lamb, F.K., Markovic, D., & Shapiro, S.L. (2001), Phys. Rev. D, 64,104014
- Rezzolla, L., Ahmedov, B.J. & Miller, J.C. (2001), MNRAS, 322, 723
- Ruderman, M. (1991a), ApJ, 366, 261
- Ruderman, M. (1991b), ApJ, 382, 576
- Ruderman, M. (1991c), ApJ, 382, 587
- Sang, Y. & Chanmugam, G. (1987), ApJ, 323, L61
- Shapiro, S.L. & Teukolsky, S.A. (1983), *Black holes, white dwarfs & neutron stars: the physics of compact objects* (New York: John Wiley)
- Shapiro, S.L. (2000), ApJ, 544,397
- Shibata, M. & Uryu, K. 2000, Phys. Rev. D, 61, 064001
- Spruit, H.C. 1999, A&A, 349, 189
- Spruit, H.C. & Phinney, E.S. 1998, Nature, 393, 139
- Srinivasan, G., Bhattacharya, D., Muslimov, A.G., Tsygan, A.I. (1990), Curr. Sc., 59, 31
- Tassoul, J.-L. (1978), *Theory of rotating stars*, (Princeton: Princeton University Press)
- Thompson, C., & Duncan, R. 1993, ApJ, 408, 194
- Urpin, V. & Geppert, U. (1995), MNRAS, 275, 1117
- Urpin, V. & Geppert, U. (1996), MNRAS, 278, 471
- Vivekanand, M. & Narayan, R. (1981), J. Astrophys. Astr., 2, 315
- Zanotti, O., & Rezzolla, L. 2002, MNRAS, 331, 376
- Zwinger, T., & Muller, E. 1997, A&A, 320, 209

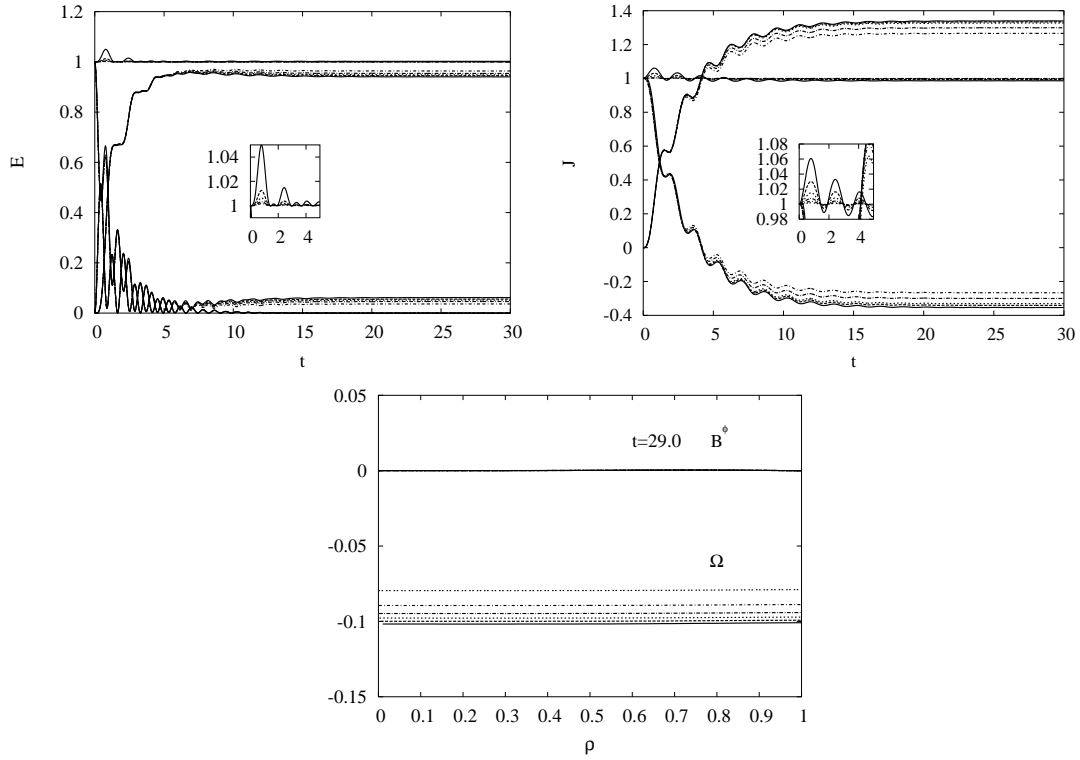


Fig. 4. Convergence tests: For the monopolar field case, plasma exterior. In the top left panel is displayed the energy conservation, the right one displays angular momentum conservation while the bottom panel contains the Ω and B^φ profiles at time $t = 29$. In all panels, the solid, the dashed, the short-dashed, the dot-dashed, the dot-short-dashed and the dotted lines indicate resolutions of 51, 101, 201, 401, 801 and 1601 points respectively.

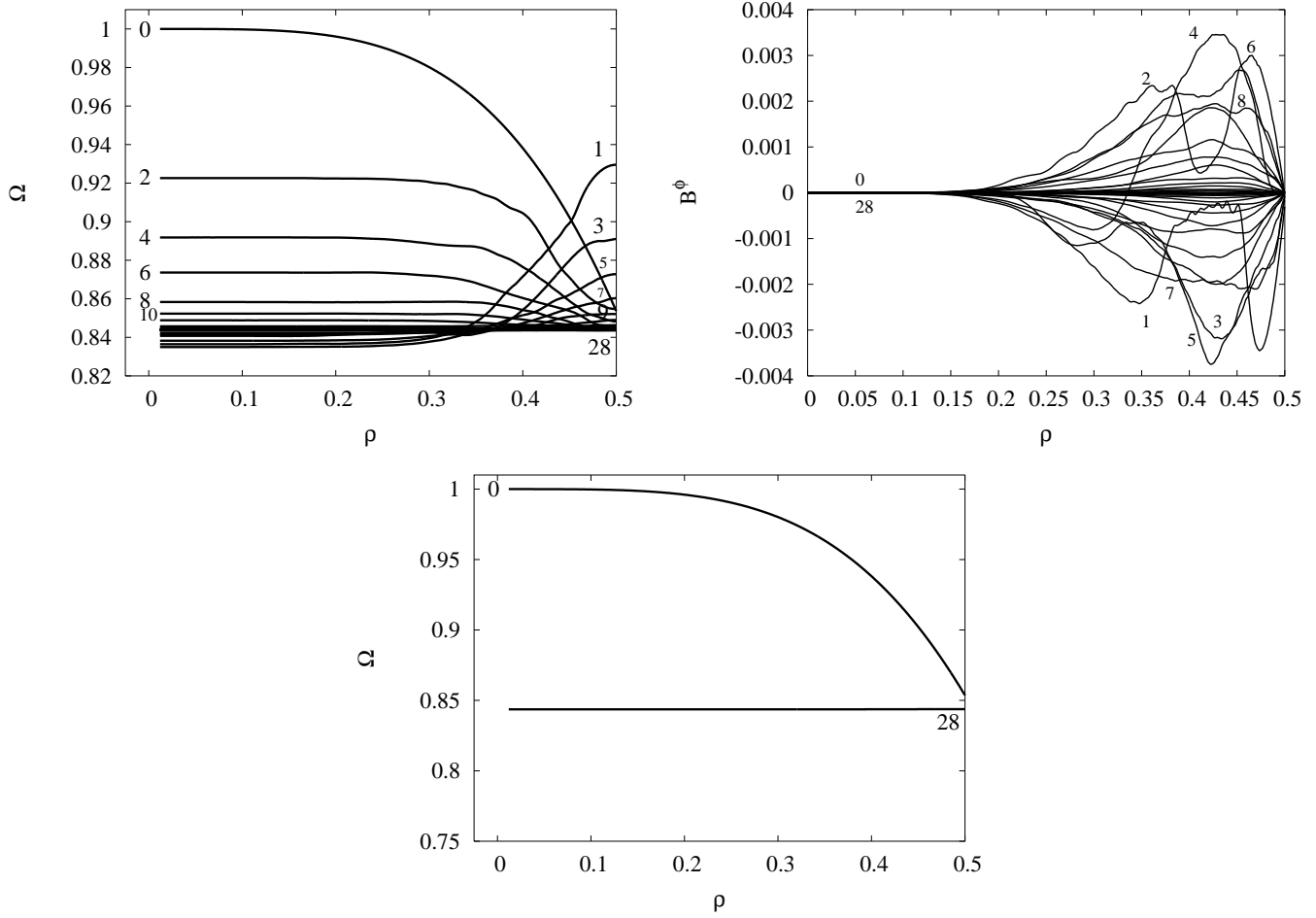


Fig. 5. Ω and B^ϕ variation for the $q = 0.3$ case. The first panel shows the variation of Ω as a function of the cylindrical coordinate ρ with time (the topmost curve being the initial curve and the rest the subsequent evolution). The second panel displays B^ϕ as a function of ρ with time (the initial and final profiles is a null profile and is hidden by the subsequent and earlier evolution respectively). The third panel shows the initial and final profile of Ω with ρ . The numbers labelling the curves in this and other figures stand for the corresponding time t ; in this figure, since the curves get very close together at late times, we suppress labelling between $t = 8$ and $t = 28$.

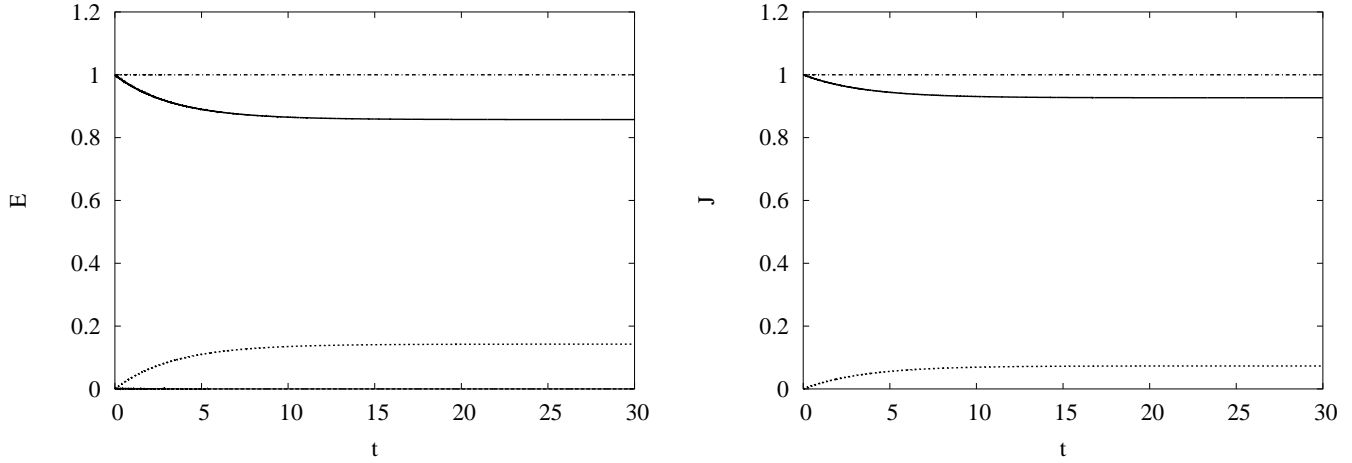


Fig. 6. Energy and angular momentum conservation for the $q = 0.3$ case. The left panel displays the energy conservation: the solid line is E_{rot} , the long-dashed line (coincident with the x -axis) represents E_{mag} , the short-dashed line is E_{Poy} and the dot-dashed line is the sum of all these quantities (all energies are normalised to the initial value of E_{rot}). The right panel displays the angular momentum conservation: solid curve is J_{rot} (see text) while the short-dashed curve is the J_{Poy} and the dot-dashed line is the sum (all scaled to the initial J_{rot}).

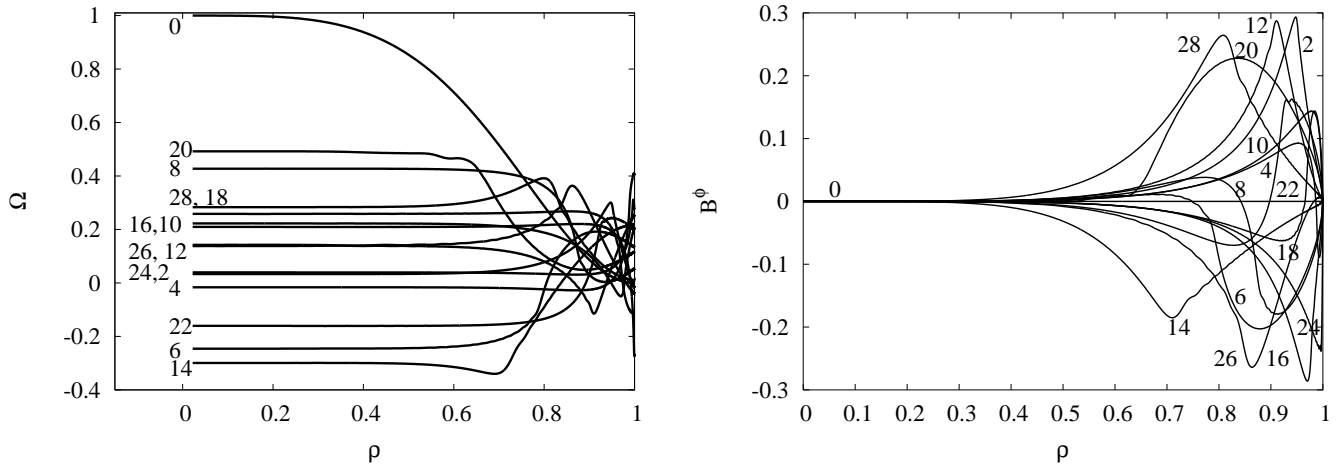


Fig. 7. Ω and B^φ variation for the $q = 0.6$ case. The curves have the same meaning as for Fig. 5 except that because $q = 0.6$ is a closed field line, the oscillations are sustained.

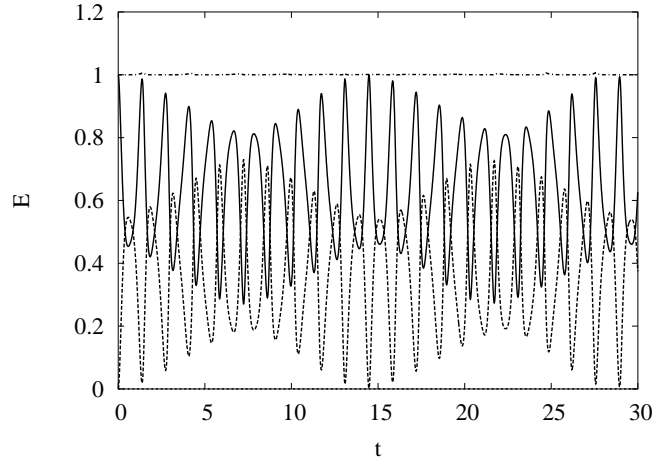


Fig. 8. Energy conservation for the $q = 0.6$ case. The curves have the same meaning as Fig. 6.

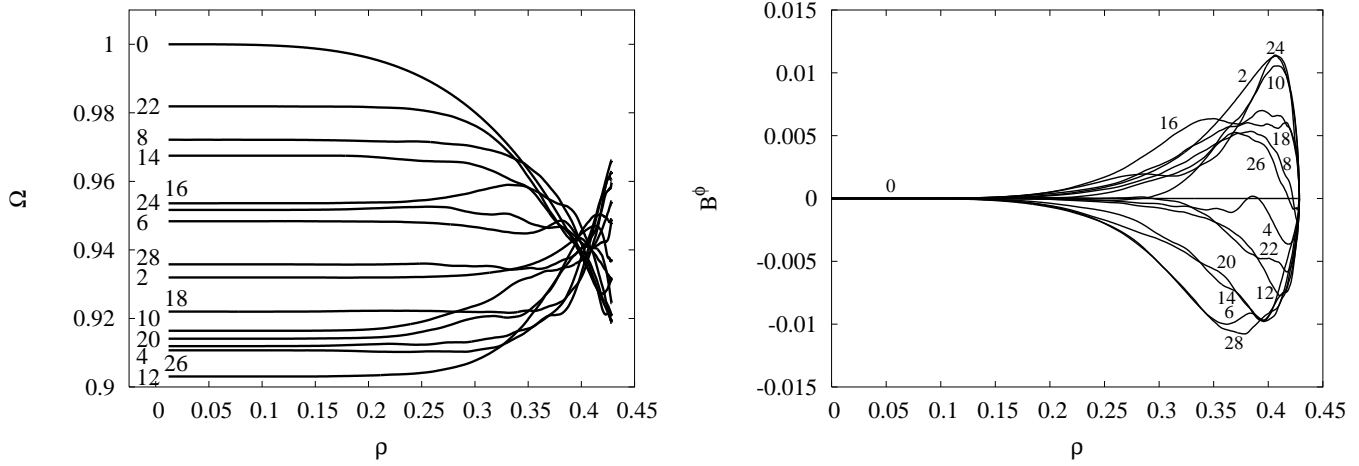


Fig. 9. Ω and B^ϕ variation for the $q = 0.8$ case. The curves have the same meaning as for Fig. 5 and dynamics almost identical to that for $q = 0.6$.

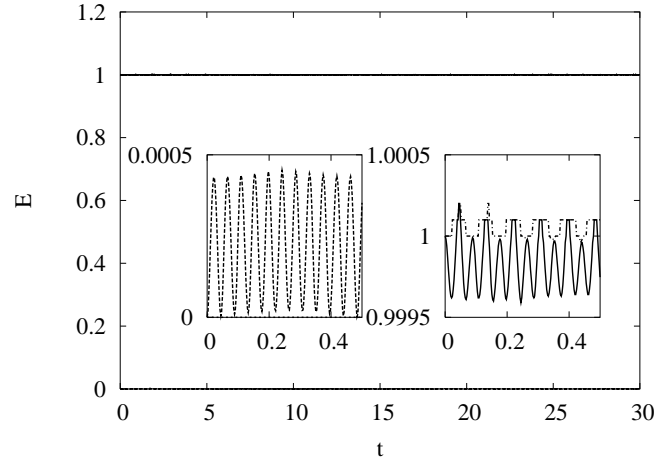


Fig. 10. Energy conservation for the $q = 0.8$ case. The curves have the same meaning as Fig. 8.

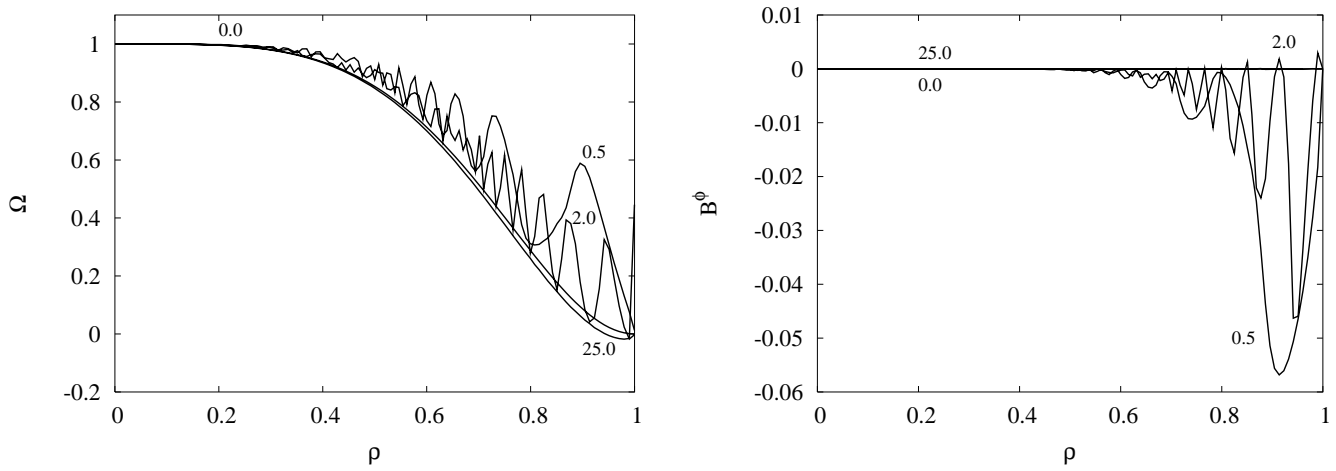


Fig. 11. Ω and B^ϕ variation at the surface. The curves have the same meaning as for Fig. 5. Structures form but do not build up due to the radiating away of the Poynting Flux. However, the dynamics at the equatorial surface (last point) do not cease due to this being a ‘closed’ field line.

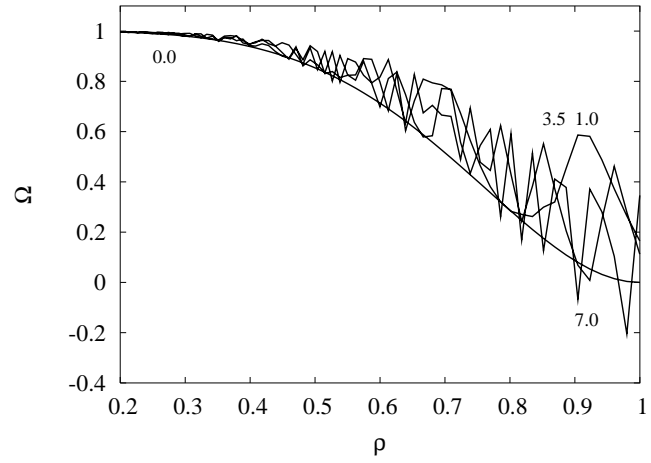


Fig. 12. Ω variation at the equator; B^φ is zero. Unlike the case for the surface, structures build up over time to a point where ‘phase-mixing’ become important.